Active Control of Rotordynamic Instability in Turbomachinery

Simon E. Mushi*
Charles L. Brown Dept. of Electrical Engineering
University of Virginia
Charlottesville, Virginia, U.S.A.

Zongli Lin
Charles L. Brown Dept. of Electrical Engineering
University of Virginia
Charlottesville, Virginia, U.S.A.

Paul E. Allaire
Dept. of Mechanical and Aerospace Engineering
University of Virginia
Charlottesville, Virginia, U.S.A.

Abstract

The onset of rotordynamic instability is a significant challenge to successful design and operation of high speed rotating machinery particularly gas compressors. The use of active magnetic bearings (AMBs) to support gas compressor rotors presents an ideal opportunity for the exploration of optimal and robust active vibration control algorithms. A notable advantage of AMBs is their ability to generate optimal support stiffness and damping characteristics. Unlike passive mechanical bearings, the support characteristics of AMBs may be modified over the operating life of the system without any major hardware changes. The objective of this paper is to demonstrate the expansion of the stability region for an experimental rotor subject to destabilizing cross-coupled stiffness. A model-based control paradigm was followed to develop nominal and uncertain dynamic models of the rotor-bearing system. Using μ-synthesis several robust controllers were designed and implemented on the MBTRI hardware to investigate their effect on the stability threshold. The best controller established a thirty-six percent increase in the stability threshold over an existing benchmark controller. This represented an increase from fifty-six percent of the maximum achievable stability threshold to seventy-six percent. A damping ratio estimation algorithm was used to experimentally evaluate the sensitivity of the various controllers to varying cross-coupled stiffness.

1 Introduction

Increased operating efficiency, higher discharge pressure ratios and reduced package size are driving a trend towards slender and higher speed rotor designs in many turbomachine applications. With centrifugal compressors, in particular, the demand for higher rotational speeds and pressures requires multiple impeller stages (and interstage seals) which leads to longer, more flexible rotors which are more prone to aerodynamic instability [1, 2]. The primary design issue with high-pressure compressors is the trade-off between rotordynamic stability and thermodynamic performance [3]. A rotor optimized for rotordynamic stability, i.e., heavy and rigid, tends to have poor aerodynamic performance, whilst a light and flexible rotor optimized for aerodynamics tends to have poor rotordynamics. Furthermore, higher pressure machines require aptly sized balance piston seals to partly offset the aerodynamic thrust load. The destabilizing influence of the balance piston on rotordynamics increases with pressure [4]. Machine stability concerns may impact project schedules, reduce production rates and cause machine and plant damage in the event of instability.

Faced with rotordynamic instability in a machine with passive bearings, the only alternative is a physical redesign of the rotor, bearings and/or seals to improve the overall damping characteristics. This highlights a major advantage for the application of active magnetic bearing (AMB) technology - the ability to modify the control algorithms at any time to provide optimal damping to stabilize

*Contact Author Information: sem5t@virginia.edu

rotor behavior [5]. The advantages of implementing an AMB system include, but are not limited to: complete elimination of oil-based lubrication systems, low parasitic power loss, direct control of the rotordynamics, lower maintenance costs and longer system life [6]. For these reasons, the use of AMBs in turbomachinery applications for oil and gas production provides clear technical and economic advantages over fluid film bearings [7]. AMB technology paves a path to introduce active vibration control to the problem of rotordynamic instability. For this application, the potential benefits of feedback are the enabling of optimal performance of the compression system as the operating conditions change over the life of the machine, and a reduction in the effects of disturbances on the system [8]. In this study, structured uncertainty descriptions of the cross-coupled stiffness force (a standard linear parametrization of the forces contributing to rotordynamic instability), and the effect of operating speed on the rotordynamics were developed. Using mixed-sensitivity optimization [9] and complex μ-synthesis [10], controllers with varying degrees of robustness to changes in the destabilizing force and operating speed were synthesized.

2 Test Rig Description

A test rig built in the Rotating Machinery and Controls (ROMAC) Laboratory at the University of Virginia consists of a 44.9 kg solid steel rotor, approximately 1 meter long supported by noncontacting radial active magnetic bearings at four locations [11, 12, 13]. A photograph of the test cell is shown in Fig. 1 and an annotated schematic of the rotor is shown in Fig. 2. Two AMB locations (NDE and DE) are used to electromagnetically suspend the rotor under direction of the feedback controller, while the remaining two AMBs (MID and QTR) are used as exciters to impart arbitrary static or dynamic loads upon the rotor. The eddy current displacement sensor locations, and auxiliary (backup) rolling element bearing locations are also shown on the figure. The rig was designed to emulate the rotordynamic characteristics of a single stage industrial centrifugal compressor operating above its first bending natural frequency. This bending mode is located at 224 Hz (13,433 rpm) in the free-free case, and the maximum speed of the motor is 300 Hz or 18,000 rpm. Subsequent free-free rotor bending modes are at 549 Hz (32,915 rpm) and 982 Hz (58,920 rpm). An embedded controller based on the Texas Instruments C6713 digital signal processor (DSP) is used to execute the control algorithms with a 12 kHz sample rate. The pair of additional radial AMBs used to provide different types of excitation are a unique aspect of the test rig. The mid span AMB (MID) induces rotordynamic instability by generating a cross-coupled stiffness force F_{xc} using feedback of the rotor position [14]

$$F_{\mathrm{xc}} = \begin{bmatrix} f_x \\ f_y \end{bmatrix} = Q \begin{bmatrix} 0 & 1 \\ -1 & 0 \end{bmatrix} \begin{bmatrix} q_x \\ q_y \end{bmatrix}, \tag{1}$$

where f_x, f_y and q_x, q_y are forces and displacements along the x and y axes respectively, and Q is the magnitude of the cross-coupled stiffness (CCS). As Q increases there is a tendency for a forward whirl (precession of the rotor orbit at a frequency equal to rotor's lowest natural frequency) to be excited. This in turn counteracts the restorative damping force produced largely by the support bearings, and can lead to unbounded oscillations at the first critical speed of the rotor, i.e., Nc1 rigid body mode. The quarter span AMB (QTR) can also be used to provide a CCS force. However, the primary function of the QTR actuator is to generate sinusoidal excitations of different amplitude and frequency so as to measure the damping ratio of Nc1 [15].

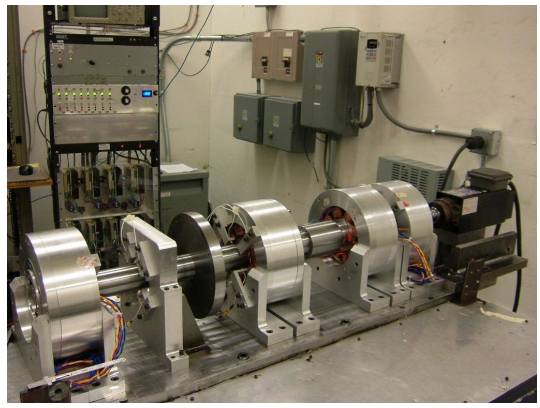

Figure 1: Photgraph of the test rig

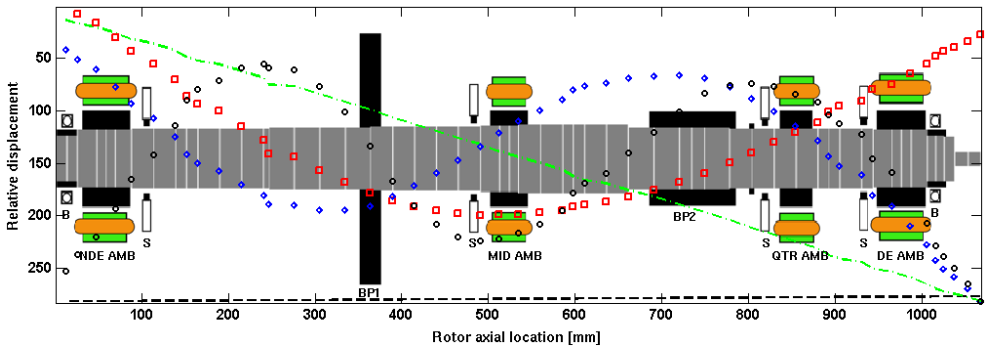

Figure 2: Rotor schematic showing axial locations of components and boundaries of the finite element stations. Position sensor are marked *S*, auxiliary bearings are marked *B*, and two balance planes are marked *BP1* and *BP2*. The relative displacements of the free-free mode shapes Nc1 (−−), Nc2 (−.−), Nc3 (□), Nc4 (◇), and Nc5 (○) are also shown.

3 Modeling

3.1 Nominal plant model

A brief treatment of the rotor and AMB modeling follows, however, the curious reader may consult [6] and references therein for a detailed treatment. The modeling commences with a finite element rotor model consisting of 50 nodes each with four degrees of freedom. Representing this high fidelity model in state space form would require 400 states. The modal truncation of the rotor model to include the rigid body modes plus the first three bending natural frequencies achieves a trade-off between requirements for an accurate and low order model. Sufficient accuracy is required to capture the relevant dynamics over the operating speed range, while a reduced-order model eliminates complexity that may result in numerical challenges during control synthesis. A magnetic circuit model is constructed to calculate the linearized AMB properties of open-loop stiffness K_x and current gain K_i. These properties are confirmed with planar magnetostatic finite element analysis. The MIMO rotor-AMB model has 20 modal states, x_r, and a state space description

$$\begin{aligned} \dot{x}_r(t) &= (A_r + B_r K_x C_{r,m})\, x_r(t) + G_{\text{amp}} B_r K_i u(t), \\ &:= \hat{A}_r x_r(t) + \hat{B}_r u(t), \qquad (2) \\ y_r(t) &= C_{r,s} x_r(t), \qquad (3) \end{aligned}$$

where A_r is the rotor state matrix, B_r is force input matrix, $C_{r,m}$ is the rotor displacement output matrix at the AMB locations, $C_{r,s}$ is rotor displacement output matrix at the sensor locations (in general, $C_{r,s} \neq C_{r,m}$), and G_{amp} is the amplifier DC gain of 2.5 A/V. The model accepts 4x1 input vector in volts and outputs a 4x1 displacements vector $y(t)$ in meters. The gain plus time delay model for the electrical and electronic components has 16 states, x_d, and a standard state space description (A_d,B_d,C_d,D_d). The output of the rotor-AMB model is the displacement at the four sensing planes which forms the input to the gain plus time delay model. The time delay models for each control channel are independent fourth-order Pade approximations that match the phase lag of the components in the signal path, i.e., power amplifiers, sensor signal conditioning filters, and DSP sampling and computational delay. The DC gain of each channel is set to be the product of individual gains of the components in the signal path. By inserting the delay model in series with the rotor-AMB model we arrive at the following compact representation of the full system requiring 36 states,

$$G(s) := \begin{bmatrix} \dot{x}_r(t) \\ \dot{x}_d(t) \\ y(t) \end{bmatrix} = \begin{bmatrix} \hat{A}_r & 0 \\ B_d C_{r,s} & A_d \\ D_d C_{r,s} & C_d \end{bmatrix} \begin{bmatrix} x_r(t) \\ x_d(t) \end{bmatrix} + \begin{bmatrix} \hat{B}_r \\ 0 \\ 0 \end{bmatrix} u(t). \qquad (4)$$

3.2 Uncertainty description

3.2.1 Rotating speed

The Campbell diagram in Fig. 3 shows changes in the rotor eigenvalues caused by the gyroscopic effect as a function of operating speed. In the figure, the 1X line denotes the speed of the rotor and intersections with the eigenvalue trajectories denote resonance. Closed-loop stability and performance is most sensitive to variations in the frequency of the lightly damped rotor bending modes within the control bandwidth. Therefore, real structured uncertainties were used to cover their range in the least conservative way, i.e. by using eigenvalue perturbation regions [16].

3.2.2 Destabilizing cross-coupled stiffness

The CCS scalar Q from (1) was defined as a real uncertain parameter. As with the rotating speed, it was observed that modeling the stiffness directly in the plant model led to unusable controllers. However, by modeling the effect of Q on the trajectory of certain system eigenvalues instead, several successful controllers were produced. The latter approach yields plant models that are less complex from a numerical standpoint. Assuming a complex eigenvalue for Nc1 of the form $\sigma \pm j\omega$, the effect of CCS on σ can be modeled either:

1. as a real-valued uncertainty varying from 200 to 240 rad/s with a nominal value of 220 rad/s denoted *CCS Model 3*, or

2. as a real-valued uncertainty varying from 200 to 260 rad/s with a nominal value of 230 rad/s denoted *CCS Model 4*.

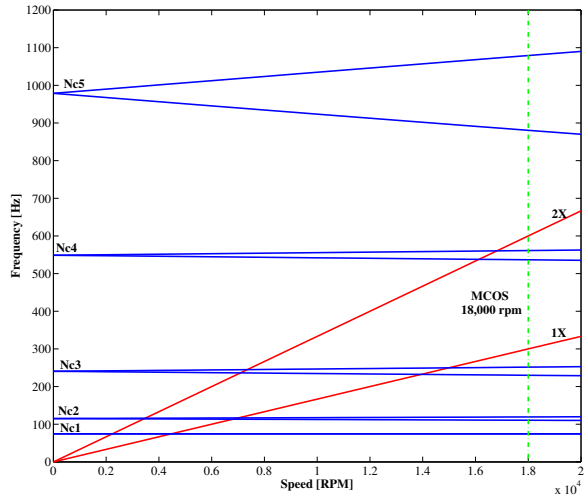

Figure 3: Campbell diagram showing splitting of eigenvalues due to increased gyroscopic effect at higher speeds.

4 Control Design

4.1 Framework

A concise discussion of the control design methodology follows, further details are discussed in [13]. The four block mixed-sensitivity problem as described in [17, 18] provides the framework for including the closed-loop performance specifications in the control problem. Frequency domain weighting functions were used to define bounds on several closed-loop system sensitivity functions. A set of benchmark weighting functions were defined and manually optimized. Using the benchmark weights as a starting point, nondiagonal performance weights were introduced as they have shown promise in maximally exploiting the available degrees of freedom during μ-synthesis [19]. Finding a suitable form of the performance weight transfer function matrix is tedious given the large parameter space to be searched. Therefore, a heuristic approach was followed to narrow the search task. The first step was the development of prototype nondiagonal scalings to systematically evaluate the effects of coupling and directionality between the four control channels: $W_{p,1}$ full-block and $W_{p,4}$ block diagonal with scaled off-diagonal terms

$$W_{p,1}(s) = \begin{bmatrix} 1 & 1 & 1 & 1 \\ 1 & 1 & 1 & 1 \\ 1 & 1 & 1 & 1 \\ 1 & 1 & 1 & 1 \end{bmatrix} \text{blkdiag}\left[W_{p,NDEx}, W_{p,DEx}, W_{p,NDEy}, W_{p,DEy}\right], \text{ and} \tag{5}$$

$$W_{p,4}(s) = \begin{bmatrix} 1 & 0.5 & 0 & 0 \\ 0.5 & 1 & 0 & 0 \\ 0 & 0 & 1 & 0.5 \\ 0 & 0 & 0.5 & 1 \end{bmatrix} \text{blkdiag}\left[W_{p,NDEx}, W_{p,DEx}, W_{p,NDEy}, W_{p,DEy}\right], \tag{6}$$

where $W_{p,NDE}(s)$ and $W_{p,DE}(s)$ are performance weights on the nondriven and driven end AMBs.

The effect of bearing stiffness anisotropy on the stability threshold has been studied in fluid-film bearings by several workers [20, 21]. The accepted observation is that increasing the difference between the vertical and horizontal principle direct support stiffness (k_{xx} and k_{yy}) leads to asymmetric whirl orbits. Compared to circular whirl orbits, asymmetric orbits are less effective at destabilizing Nc1. The result is a higher instability threshold. However, the drawback is a larger synchronous response amplitude along the axis with reduced stiffness [22]. Anisotropy χ was introduced by weighting the control sensitivity function more heavily for one axis, i.e., the y axis has 70% the stiffness of the x axis.

4.2 Synthesis Results

A total of seven controllers were synthesized from the set of performance weights discussed above and the uncertainty models. Four of these controllers were designed using only the rotating speed uncertainty model: benchmark I, 70% anisotropy, block diagonal $W_{p,4}$, and full block $W_{p,1}$. Two of the remaining were designed using the speed and *CCS Model 3* uncertainty descriptions: benchmark Ic3 w/Model CC3, and block diagonal $W_{p,4}$ w/Model CC3. The final controller was designed with the speed and *CCS Model 4* uncertainty descriptions and was denoted block diagonal $W_{p,4}$ w/Model CC4. The benchmark I controller had 48 states and a μ upper bound of 1.02. Fig. 4 shows a singular value plot of the benchmark controller as well as the uncertain plant model used during synthesis. Under the benchmark controller, the test rig was able to operate to its maximum speed of 18,000 rpm.

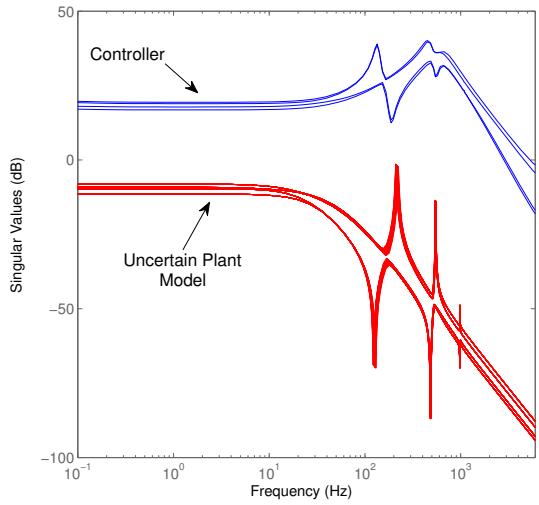

Figure 4: Singular value plot of benchmark controller and uncertain plant model.

5 Experimental Results

5.1 Stability threshold determindation

The stability of the first rigid body rotor mode Nc1 is strongly affected by the destabilizing CCS added to the rotor-AMB system. We are interested in determining which combination of performance weights and uncertainty models can maximize the magnitude of CCS required to drive the closed-loop unstable. Instability is considered in the linear asymptotic case, i.e., once the damping ratio of Nc1 becomes zero. The maximum value of CCS prior to the onset of instability is denoted the stability threshold.

To experimentally determine this threshold, successively higher levels of CCS were applied using the midspan AMB. The CCS reduces the damping of the eigenvalue corresponding to Nc1 by encouraging forward whirl. The damping ratio of Nc1 can be estimated from the free decay of rotor vibration at the natural frequency of Nc1.

Circular sinusoidal excitation was provided by driving the quarter span radial AMB in open-loop mode. The excitation frequency and direction (forward or backward) was varied so as to target the precise frequency of Nc1. This is known as blocking [15]. The free decay of the rotor vibrations following the termination of the blocking excitation was recorded from multiple position sensors using a separate data acquisition system. The time-domain data was processed offline using a backward auto-regression algorithm written to extract the natural frequency and damping ratio information [23].

5.2 Cross-coupled stiffness sensitivity

The Nc1 log decrement ζ_1 was measured over a range of CCS magnitudes from zero up to the onset of instability to ascertain the sensitivity of the rotor-bearing system stability. For a given controller and CCS magnitude, the mean log decrement was calculated by averaging the output of five decays measured at the four support bearing displacement sensors, i.e. a total of 20 samples. The stability maps in Figs. 5a and 5b reveal the resulting trend and statistics. The standard deviations of the log decrement (as indicated by the error bars) tend to be larger at lower CCS values since the decay is much shorter given higher damping ratios. The maximum allowable CCS $Q_{\max}$ assuming optimum support damping (as derived from [1]) was 3540 N/mm and is shown as a dashed vertical line. From the data presented the following conclusions were drawn for the controllers designed without CCS uncertainty descriptions:

1. The controller designed with block-diagonal performance weight $W_{p,4}$ extended the stability threshold by 30%, the largest increase for controllers synthesized without a CCS uncertainty model.

2. The controller designed with 70% support stiffness anisotropy increased the stability threshold by only 18% from the benchmark. However, this controller had the largest effect on the Nc1 log dec in the absence of cross-coupling. At Q=0, this controller achieved a log dec of 3.5 versus 2.2 for Benchmark I, a 59% increase.

3. Increased levels of stiffness anisotropy did not lead to improvements in the stability threshold. The 50% support stiffness controller had different stability thresholds depending the direction of impulse excitation, 2300 N/mm in the $x-$axis and 730 N/m in the $y-$axis.

4. The full block diagonal $W_{p,1}$ controller has a log decrement curve below the Benchmark I controller for all values of Q. The stability threshold of this controller was 33% lower than the benchmark.

With the inclusion of CCS uncertainty description the following conclusions were drawn for the controllers synthesized:

1. Benchmark Ic3 achieves a log decrement of 4.0 the highest log decrement among all controllers at $Q = 0$. However, the stability threshold of the controller is 15% lower than Benchmark I.

2. The controllers designed with the block diagonal $W_{p,4}$ performance weight achieve thresholds of 2500 N/mm and 2700 N/mm, i.e., the third highest and highest, when using *CCS Models 3* and *4,* respectively. Surprisingly, *CCS Model 3* has the higher threshold despite defining a smaller eigenvalue perturbation than *CCS Model 4*. Also, the log dec curve associated with *CCS Model 4* remains below all the other controllers up to 1500 N/m.

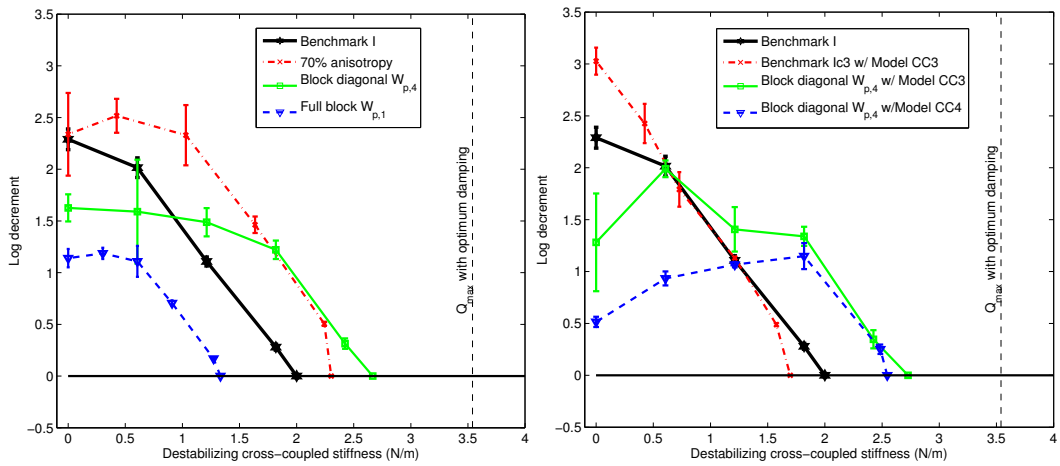

(a) Without CCS uncertainty model (b) Including CCS uncertainty model

Figure 5: First rotor mode stability as a function of destabilizing CCS

6 Conclusion

A test rig to demonstrate the active control of rotordynamic instability using active magnetic bearings has been successfully commissioned. Using frequency domain weighting functions, the engineering specifications of stability and robustness have been translated into cost functions to be optimized by the robust controller synthesis procedure. Several robust μ-synthesis controllers were designed to safely suspend the rotor as it is operated from 0 to 18,000 rpm, crossing one bending natural frequency. Using experimental damping ratio measurement techniques, the stability sensitivity as a function of the destabilizing force was determined. With the highest performing controller, the stability threshold was demonstrated to be 36% higher than initial benchmark value, i.e., the onset of instability has been delayed until the disturbance force increased by 36%. This brings us to within 76% of the maximum allowable instability $Q_{\max}$ assuming the presence of optimum damping. The extent to which the threshold may be further increased is under continued investigation.

References

[1] L. Barrett, *Stability and Nonlinear Response of Rotor-bearing Systems with Squeeze Film Bearings*. PhD thesis, University of Virginia, 1979.

[2] J. Moore, M. Camatti, A. Smalley, G. Vannini, and L. Vermin, "Investigation of a rotordynamic instability in a high pressure centrifugal compressor due to damper seal convergence," in *Proc. 7 th IFToMM Conf. on Rotor Dyn.*, 2006.

[3] U. Baumann, "Rotordynamic stability tests on high-pressure radial compressors," in *Proc. of 28th Turbomachinery Symp.*, (Texas A&M University, College Station, TX), 1999.

[4] J. Moore and D. Ransom, "Centrifugal compressor stability prediction using a new physics based approach," *ASME J. Eng. Gas. Turb. Power*, vol. 132, no. 8, p. 082402, 2010.

[5] H. Habermann and M. Brunet, "The active magnetic bearing enables optimum damping of flexible rotor," *ASME Paper 84-GT-117*, 1984.

[6] G. Schweitzer and E. Maslen, eds., *Magnetic Bearings: Theory, Design, and Application to Rotating Machinery*. Springer, 2009.

[7] M. Ahrens, B. Frei-Spreiter, and R. Wieser, "Cost efficient electric high-speed drives with magnetic bearings for the COG market," in *Proc. 7th Int. Symp. Magn. Brgs. ISMB7*, pp. 507–512, 2000.

[8] J. Doyle, B. Francis, and A. Tannenbaum, *Feedback Control Theory*. Macmillan Publishing Company, 1990.

[9] A. Iqbal, Z. Wu, and F. Ben Amara, "Mixed-sensitivity H_∞ control of magnetic-fluid-deformable mirrors," *IEEE/ASME Trans. Mech.*, vol. 15, no. 4, pp. 548–556, 2010.

[10] E. Maslen and J. T. Sawicki, "Mu-synthesis for magnetic bearings: why use such a complicated tool?," in *Proc. ASME Int. Mech. Engr. Congr. Expo IMECE2007*, no. 43033, pp. 1103–1112, 2007.

[11] S. Mushi, Z. Lin, and P. Allaire, "Stability analysis of a flexible rotor on active magnetic bearings subject to aerodynamic loads," in *Proc. 12th Int. Symp. Magn. Brgs. ISMB 12*, (Wuhan, China), 2010.

[12] S. Mushi, Z. Lin, and P. Allaire, "Design, construction and modeling of a flexible rotor active magnetic bearing test rig," *IEEE/ASME Trans. Mechatronics.*, vol. PP, no. 99, 2011. (to appear).

[13] S. Mushi, *Robust Control of Rotordynamic Instability in Rotating Machinery Supported by Active Magnetic Bearings*. PhD thesis, University of Virginia, May 2012.

[14] C. Cloud, *Stability of Rotors Supported by Tilting Pad Journal Bearings*. Ph.D. dissertation, University of Virginia, 2007.

[15] C. Cloud, E. Maslen, and L. Barrett, "Damping ratio estimation techniques for rotordynamic stability measurments," *ASME J. Eng. Gas Turb. Power*, vol. 131, 2009.

[16] G. Balas and J. Doyle, "Robustness and performance trade-offs in control design for flexible structures," *IEEE Trans. Contr. Syst. Technol.*, vol. 2, pp. 352–361, Dec. 1994.

[17] M. Englehart and M. Smith, "A four-block problem for h infin; design: properties and applications," in *Proc. 29th IEEE Conf. Decision Control*, vol. 4, pp. 2401–2406, 1990.

[18] U. Schonhoff, *Practical Robust Control of Mechatronic Systems with Structural Flexibilities*. Ph.D. dissertation, Darmstadt Technical University, 2002.

[19] M. Boerlage, *Rejection of Disturbances in Multivariable Motion Systems*. Ph.D. dissertation, Eindhoven University of Tehnology, 2008.

[20] D. Childs, *Turbomachinery Rotordynamics: Phenomena, Modeling, and Analysis*. Wiley, 1993.

[21] F. F. Ehrich, *Handbook of Rotordynamics*. Krieger Publishing Company, 2004.

[22] J. Vance, F. Zeidan, and B. Murphy, *Machinery Vibration and Rotordynamics*. Wiley, 2010.

[23] R. Kumaresan and D. Tufts, "Estimating the parameters of exponentially damped sinusoids and pole-zero modeling in noise," *IEEE Trans. Acoust. Spch. Signal Proc.*, vol. 30, no. 6, pp. 833–840, 1982.